MAGNETISM

Orbital magnetoresistance in the antiferromagnet CoO driven by dynamic orbital angular momentum

Christin Schmitt[1], Sachin Krishnia[1]*, Mahmoud Zeer[2], Edgar Galíndez-Ruales[1], Mehak Loyal[1], Jonas Köhler[1], Luca Micus[1], Takashi Kikkawa[3,4], Hiroki Arisawa[3,5], Thibaud Denneulin[6], András Kovács[6], Renyou Xu[1,7], Duc Tran[1], Florian Kronast[8], Dongwook Go[1,2,9], Leonid V. Pourovskii[10,11], Rafal E. Dunin-Borkowski[6], Timo Kuschel[1,12], Marjana Ležaić[2], Jairo Sinova[1,13], Eiji Saitoh[3,5,14,15], Gerhard Jakob[1], Olena Gomonay[1], Yuriy Mokrousov[1,2], Mathias Kläui[1,16]*

Recent predictions of orders of magnitude larger orbital current effects compared with spin currents have attracted considerable interest. However, orbital currents must first be converted into spin currents to interact with the static magnetization dominated by spin angular momentum in conventional magnets. By using a magnet dominated by orbital angular momentum (OAM), we demonstrate a 70-fold enhancement in orbital Hall magnetoresistance in cobalt II oxide/copper (CoO/Cu*), compared with spin Hall magnetoresistance in cobalt II oxide/platinum (CoO/Pt). This arises from interactions between dynamic OAM from surface-oxidized Cu* and static OAM in the antiferromagnetic insulator CoO. Our results show how by using OAM-dominated materials, we can harness the benefits of giant orbital currents that have not been possible using conventional spin-dominated magnets.

In recent decades, the interaction between static magnetization and the flow of spin angular momentum (spin currents), has been employed as the key mechanism to detect and control the magnetic state of ferromagnets. This interaction has enabled major applications, ranging from giant magnetoresistive sensors (*1*, *2*) to spin-orbit torque magnetic random-access memory (*3*, *4*), chiral skyrmion–based racetrack memory (*5*, *6*), logic devices (*7*), and neuromorphic applications (*8*–*10*). However, the generation of spin current relies heavily on the spin-orbit coupling (SOC) of materials, which is a weak relativistic effect that limits the efficiency and constrains materials choices (*11*). More recently, the dynamic orbital angular momentum (OAM)—the counterpart of electron spin angular momentum—has emerged as a promising alternative to manipulate magnetization more efficiently (*12*–*16*). Two mechanisms of orbital current generation are orbital Hall effect (OHE) in the bulk (*13*, *17*, *18*) and orbital Rashba Edelstein effect (OREE) at interfaces (*19*, *20*), analogous to their spin counterparts (*21*). Unlike spin currents, whose generation from charge currents relies on the relatively weak SOC mechanism, orbital currents can be directly generated from charge currents because the crystal momentum of charge carriers (e.g., electrons) can directly couple to OAM. This results in a more robust, orders-of-magnitude larger generation of current-induced OAM (orbital currents), even in light, abundant, inexpensive, and environmentally friendly materials (*13*, *22*–*25*). Despite these advantages, the fundamental limitation in utilizing orbital currents for device applications lies in their low interaction efficiency with magnetization that in conventional transition metals is carried by spin angular momentum. Whereas spin currents interact efficiently with magnetization (or spin moments) through strong *s-d* exchange interaction, orbital currents cannot couple in conventional magnetic materials with nearly quenched OAM by any strong exchange interaction, and therefore one cannot make use of the large orbital currents to effectively interact with conventional spin-based magnets.

To address this issue, the mitigation strategy has been the conversion of orbital currents into spin currents using materials that exhibit high SOC (*14*, *26*). However, the efficiency in such cases again relies on the comparably weak relativistic SOC mechanism in the conversion layer. This approach achieves a modest enhancement in spin torque efficiency, typically a fewfold (*14*, *27*–*29*), which is considerably smaller than the theoretically predicted orders of magnitude enhancement.

Therefore, to fully exploit the potential of large orbital currents, one needs to directly couple it with orbital magnetization carried by OAM (orbital magnetism), thus bypassing the need for inefficient orbital-to-spin conversion. Recent theoretical studies predict that orbital-orbital interactions can be a sizable fraction of the *s-d* exchange interaction, indicating that the role of orbital exchange could be considerable (*30*). Antiferromagnetic (AFM) transition metal oxide insulators can exhibit strong orbital magnetization as well as THz spin dynamics (*31*, *32*), immunity to external magnetic fields enhancing stability, and low damping, which allows for the transport of angular momentum over long distances (*33*, *34*). By exploiting the interaction between orbital currents from Cu* and unquenched orbital magnetization in CoO, we demonstrate an enhancement of two orders of magnitude in the magnetoresistance (MR) in CoO/Cu* bilayers compared with conventional spin-based CoO/Pt.

Spin and OHE magnetoresistance

We use CoO, a collinear insulating AFM, for which the OAM of each Co atom is sizable (≈ 2.05 μ_B/atom) (*35*), unlike in *3d* transition metal ferromagnets for which orbital moments are nearly fully quenched (<0.1 μ_B/atom) (*36*–*38*). Thus, CoO serves as an ideal system to investigate the interaction between orbital currents and orbital magnetization and to distinguish it from spin magnetization effects. The insulating nature of CoO is particularly suitable as it allows us to rule out effects of current flow in the magnet such as self-torques or anisotropic MR effects (*39*, *40*). The collinear magnetic and crystallographic structure of CoO is shown in Fig. 1A.

We deposited epitaxial CoO (5 nm) / Pt (2 nm) and CoO (5 nm)/Cu* (6 nm) thin films on MgO(001) substrates using reactive magnetron sputtering [see section S1.1 (*41*)]. Here, the asterisk denotes the natural oxidation of Cu, which serves as an orbital current generator through the OREE (*14*), whereas Pt generates spin current through the spin Hall effect mechanism (*3*, *11*). As shown in Fig. 1A, the CoO thin films exhibit fourfold in-plane magnetocrystalline anisotropy with two magnetic easy axes of the Néel vector (***n***) oriented along the [110] and $[\bar{1}10]$ crystallographic axes (*38*, *42*, *43*).

The Néel temperature (T_N) of our thin films is approximately 300 K, slightly higher than that of bulk CoO [T_N = 291 K for bulk CoO (*44*, *45*), see sections S1.1 and S2 of (*41*)]. Scanning transmission electron

[1]Institute of Physics, Johannes Gutenberg-University Mainz, Mainz, Germany. [2]Peter Grünberg Institut (PGI-1), Forschungszentrum Jülich and JARA, Jülich, Germany. [3]Department of Applied Physics, The University of Tokyo, Tokyo, Japan. [4]Advanced Science Research Center, Japan Atomic Energy Agency, Tokai, Japan. [5]RIKEN Center for Emergent Matter Science, Wako, Japan. [6]Ernst Ruska-Centre for Microscopy and Spectroscopy with Electrons, Forschungszentrum Jülich, Germany. [7]Fert Beijing Institute, MIIT Key Laboratory of Spintronics, School of Integrated Circuit Science and Engineering, Beihang University, Beijing, China. [8]Helmholtz-Zentrum Berlin für Materialien und Energie, Berlin, Germany. [9]Department of Physics, Korea University, Seoul, Republic of Korea. [10]CPHT, CNRS, École polytechnique, Institut Polytechnique de Paris, Palaiseau, France. [11]Collège de France, Université PSL, Paris, France. [12]Faculty of Physics, Bielefeld University, Bielefeld, Germany. [13]Department of Physics, Texas A&M University, College Station, TX, USA. [14]WPI-Advanced Institute for Materials Research, Tohoku University, Sendai, Japan. [15]Institute for AI and Beyond, The University of Tokyo, Tokyo, Japan. [16]Center for Quantum Spintronics, Norwegian University of Science and Technology, Trondheim, Norway. ***Corresponding authors. Email: skrishni@uni-mainz.de (S.K.); klaeui@uni-mainz.de (M.K.)**

microscopy (STEM) and electron energy loss spectroscopy (EELS) confirm the high-quality epitaxial growth of CoO and the formation of sharp, clean, and well-defined interfaces in the CoO/Cu* system [see section S2 and figs. S2 and S3 of (*41*)]. Furthermore, the x-ray absorption (XAS) spectroscopy experiments confirm that our CoO thin films exhibit a large orbital magnetization [larger than 1 μ_B / atom; see section S3 and fig. S4 of (*41*)].

To investigate the interaction between orbital current and static OAM, we fabricated Hall bar structures 6 μm wide (see Fig. 1B for an example of CoO/Cu*) and measured orbital Hall magnetoresistance (OMR) [see section S1.2 of (*41*)]. When a charge current I is injected into the Hall bar, it generates orbital current in Cu* through OHE and/or OREE. An orbital accumulation μ_o is built up at the CoO/Cu* interface. Analogous to the spin Hall magnetoresistance (SMR) mechanism (*46*), the OMR refers to the change in electrical resistance of a nonmagnetic material caused by the interaction of orbital currents with the magnetization of an adjacent magnetic layer, governed by the orientation of the Néel vector.

Although SMR has been studied in Pt adjacent to a range of materials, including *3d* ferromagnets and insulating magnets (*46*, *47*), the reported pure OMR remains weak for the materials previously studied (*48*) primarily because there is no direct coupling to conventional spin-dominated magnetization in these materials. We first consider a CoO/Pt device to compare the interaction of spin currents with CoO to the interaction of orbital currents in CoO/Cu*. We apply an external magnetic field of 13 T along the [110] direction of CoO to align the Néel vector along the well-defined $[\bar{1}10]$ magnetic easy axis (*42*). We then sweep the magnetic field in $[\bar{1}10]$ direction and probe the reorientation of Néel vector by measuring the transverse resistance (R_{xy}) at T ($< T_N$) = 150 K. R_{xy} exhibits different behavior when the magnetic field is swept upward and downward in the range of 7.5 to 9 T (Fig. 2A). This change in R_{xy}, normalized by the longitudinal resistance ($R_{xy}/\bar{R}$), represents the spin-flop transition and rotation of the Néel vector by 90°, i.e., from $[\bar{1}10]$ to [110] in this case. The orientation of the Néel vector remains unchanged upon reducing the magnetic field to zero (*42*). Therefore, the difference in R_{xy} at zero fields, before, and after the magnetic field sweep, effectively probes the two perpendicular Néel vector orientations, providing a measure of SMR amplitudes. Furthermore, because the SMR is estimated from resistance measurements taken at zero magnetic fields, additional contributions to the MR from the metallic layers, such as Hanle magnetoresistance (*49*), can be ruled out. The amplitude of SMR ($\Delta R_{xy}/\bar{R}$) in CoO/Pt at 150 K is found to be 0.0078%. This amplitude of the SMR is on the order of what is found for combinations of Pt with magnetic insulators with spin-based magnetization such as NiO, YIG, and hematite (*46*, *50*, *51*). Based on the theory of SMR in magnetic insulators, the spin Hall angle (θ_{SH}) of 2-nm-thick Pt, with a resistivity of 26 Ω cm at 150 K, is estimated to be ≈*3.5%* with spin diffusion length λ_s ≈1.5 nm, which agrees well with previous studies (*42*) assuming a real part of the spin-mixing conductance of $G_r = 5 \times 10^{10}\ \Omega^{-1}\,m^{-2}$ (*46*).

We now compare this result with OMR measurements on the CoO/Cu* sample. Figure 2B shows the $R_{xy}/\bar{R}$ as a function of the magnetic field measured at T = 150 K (below T_N). The magnetic field protocol used is the same as that for the measurements in Fig. 2A. An abrupt change in R_{xy} is observed at the spin-flop field, which occurs at approximately 7.5 to 9 T. This value is similar to that observed for CoO/Pt, indicating that the magnetocrystalline anisotropy of CoO remains largely unaffected by the choice of metallic layer on top. The observation of MR in the absence of any substantial spin current source indicates the presence of orbital currents originating from Cu*, consistent with previous observations of OMR in Cu* adjacent to metallic ferromagnets (*48*). We observe a change in the sign of R_{xy} at the spin-flop field compared with the CoO/Pt structure, a distinct characteristic of orbital current interaction with the unquenched orbital moment in CoO not found in *3d* transition metal ferromagnets with quenched OAM (*48*). The OMR magnitude of 0.28% is ~*36* times larger than the SMR observed in CoO/Pt at 150 K.

Although Cu* has been recently identified as an efficient source of orbital current (*14*, *27*), the observed orders of magnitude higher MR in CoO/Cu* cannot be explained solely by the large orbital currents, as the magnitude of OMR in our previous results for spin-based magnets, NiFe/Cu* (0.05%) is considerably smaller than the OMR in our CoO/Cu* sample (*48*). Our experimental results thus suggest that additional factors or mechanisms must contribute to the large amplitude of the MR in the CoO/Cu* system. Specifically,

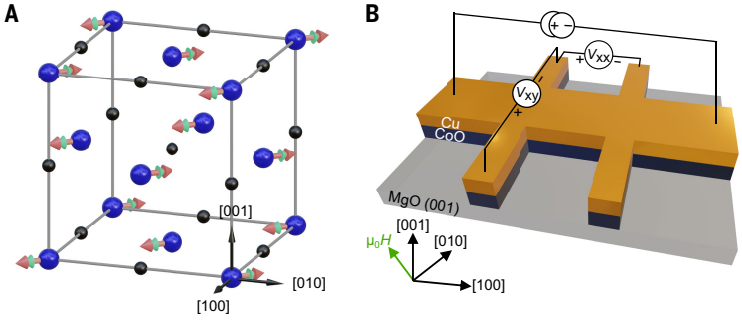

Fig. 1. Magnetic structure of CoO and experimental geometry. (**A**) Illustration of the magnetic and crystallographic structure of CoO with in-plane magnetocrystalline anisotropy, showing the Néel vector easy axis along the $[\bar{1}10]$ axis. The Co and O atoms are represented by blue and black solid circles, respectively. The red and green arrows denote the spin and orbital angular momenta of each Co atom, respectively. (**B**) Schematic of the transverse and longitudinal MR measurement schemes with electrical contacts in the CoO/Cu* structure, including the magnetic field sweep direction $[\bar{1}10]$ shown by a green arrow.

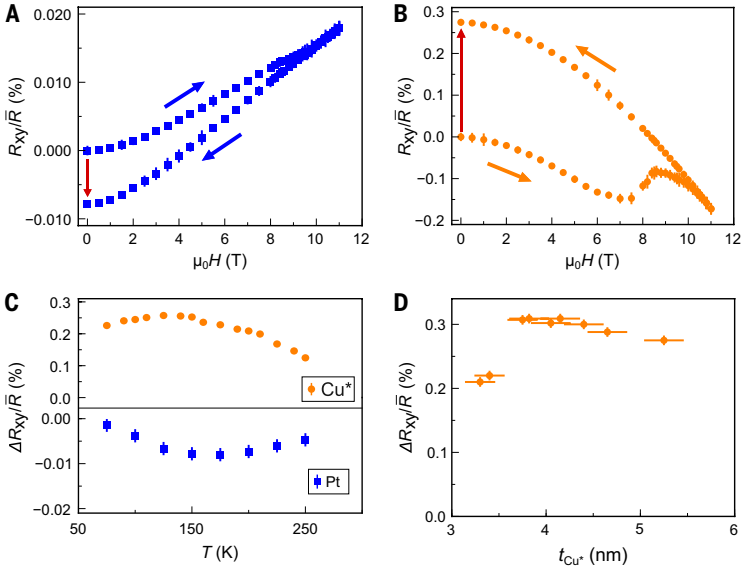

Fig. 2. Spin and orbital Hall magnetoresistance. Magnetic field sweep measurements on (**A**) CoO (5 nm) / Pt (2 nm) and (**B**) CoO (5 nm) / Cu* (6 nm) sample, respectively. Both samples exhibit a spin-flop transition between 7.5 T to 9 T. The change in transverse resistance corresponding to the two perpendicular Néel vector orientations is indicated by the red arrow for SMR in (A) and OMR in (B). The measurements are performed at T = 150 K. (**C**) The difference in transverse resistance, normalized with the longitudinal resistance for two perpendicular Néel vector states at zero field as a function of temperature. The top panel presents the results for CoO/Cu* (in orange), and the bottom panel shows the results for CoO/Pt (in blue). (**D**) The difference in transverse resistance for two perpendicular Néel vector states at zero field as a function of Cu*-layer thickness in CoO/Cu*(t_{Cu^*}). The measurements were performed at a constant temperature of T = 150 K.

our findings indicate that while spin currents from Pt interact with the spin magnetization in CoO through spin exchange coupling, the orbital current from Cu* interacts strongly with the large unquenched component of the orbital magnetization in CoO. This interaction is dominant in CoO/Cu* samples in which no considerable source of spin current is present, and is thus responsible for the relative magnitude of OMR compared with the conventional CoO/Pt. To validate this interpretation, we compare the results to the MR in α-Fe_2O_3/Cu*, for which the static OAM is quenched and we find no sizeable OMR [see section S5 and fig. S6 in (*41*)].

We next discuss the opposite sign of MR in the two systems. The sign of spin current from Pt and orbital current from Cu* is theoretically predicted (*22*) and experimentally found to be the same, as confirmed by the same sign of SMR and OMR in NiFe/Pt and NiFe/Cu* systems (*48*). However, the unquenched OAM of CoO can give rise to an orbital quadrupole moment. Our results indicate that the dynamics of the orbital quadrupole moment in CoO are fundamentally different from the classical dynamics of ferromagnets. A similar anomaly in quadrupole moment dynamics has recently been experimentally demonstrated in a noncollinear antiferromagnet, Mn_3Sn (*52*).

To understand the underlying mechanisms for the large MR magnitude and its sign, we compare the temperature dependence of the MR in the two systems. Figure 2C shows the evolution in MR as a function of temperature in CoO/Cu* (top) and CoO/Pt (bottom) showing a similar nonmonotonic behavior. The ratio of the MR in CoO/Cu* to CoO/Pt changes from 36 at 200 K to 64 at 100 K, showing that distinct mechanisms are involved. For SMR, spin relaxation by phonon scattering is important (*51*), whereas OMR is not prone to such damping mechanisms.

Origin of the orbital current

The observed orbital current could have its origin primarily in either the bulk Cu* through OHE or at the surface through OREE. To determine the origin, we perform Cu* thickness-dependent measurements of OMR in CoO/Cu*(t_{Cu*}) samples at 150 K. To investigate this within the same device, i.e., keeping the CoO/Cu* interface unchanged, we progressively reduce the Cu* layer thickness using Ar^+ ion-milling technique, followed by exposure to air for 12 hours after each etching step. The remaining Cu* thickness after each etching step was estimated by comparing the sheet resistance of the milled device to that of separately grown Cu*(t_{Cu*}) thin films [see sections S6 and fig. S7 of (*41*)]. In Fig. 2D, we show the Cu* layer thickness dependence of the OMR. The OMR remains nearly constant at ~0.32% for Cu* thicknesses ranging from 3.7 to 5.5 nm. When the Cu* thickness is reduced further to 3.2 nm, the OMR decreases slightly, from 0.32% to 0.22%. For Cu* thicknesses below 3.2 nm, the sample becomes insulating, making it impossible to measure any OMR. This trend suggests that the orbital current responsible for the OMR in our samples predominantly originates at the surface of the Cu layer, which exhibits a pronounced oxidation [see fig. S3 of (*41*)], and arises from the OREE. The enhancement of OMR observed can thus result from the efficient generation of large orbital currents at the oxidized Cu surface by OREE. Furthermore, the nearly constant OMR in the thickness range of 3.7 to 5.5 nm implies that this mechanism is robust within this thickness regime, likely owing to sufficient Cu volume and thus constant oxygen gradient and Cu* thickness.

To determine whether the larger OMR originates from the CoO layer and to rule out contributions from other effects, such as the Hanle effect and Lorentz magnetoresistance in metallic layers, we measure the angular dependence of R_{xy} for different magnetic field amplitudes. The magnetic field strengths range from values below to above the spin-flop fields of CoO. Figure 3 shows that the amplitude of the MR is nearly zero for magnetic field strengths below the spin-flop transition for both samples [see section S7 of (*41*) for details]. As the magnetic field is increased beyond the spin-flop field (8 to 9 T), the MR signal saturates, confirming that the observed effect is field-independent and ruling out the contribution from other spurious signal origins. The amplitude of the MR measured is consistent with the values obtained using the zero-field

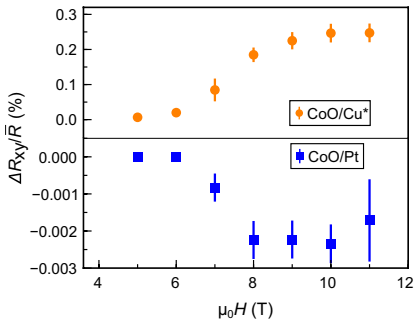

Fig. 3. External field dependence of MR. The change in transverse MR for CoO (5 nm)/Cu* (6 nm) (top) and CoO (5 nm)/ Pt (2 nm) (bottom) as a function of applied magnetic field at $T = 200$ K.

approach (see Fig. 2C) at $T = 200$ K, showing the robustness of our measurement approach and the effect. Additionally, the observed hysteresis in the transverse MR is in line with the presence of substantial unquenched OAM in our sample (*38*).

Discussion and outlook

CoO is known for its uncompensated atomic-like orbital magnetism of *d*-electrons, which arises as a result of a combination between the crystal field, band filling, and electron-electron correlation of t_{2g}-electrons (*53*, *54*). Our first-principles calculations of the AFM CoO for experimental lattice parameters predict the value of the gap of the order of 2.5 eV, with the magnitude of local spin and orbital moments of the order of 2.70 μ_B and 1.2 μ_B [see sections S3 and S8, and figs. S4 and S11 in (*41*)].

Although the insulating gap in CoO originates from strong electronic correlations, its formation can be effectively understood based on a reduced Hamiltonian incorporating orbital-dependent interaction terms that split states of opposite orbital polarization. In this sense, the correlation effects can be recast as an effective orbital exchange field acting on Co 3*d*-manifold of states, providing an intuitive single-particle picture of the gap formation [see section S10 of (*41*)].

To probe the response properties of CoO to injected spin and orbital currents, we performed first-principles linear response calculations [see section S9 of (*41*)] of the spin and orbital moments, S_i and L_i, respectively, as well as orbital quadrupoles $\{L_i, L_j\}$, induced by applied spin and orbital exchange fields, which can mimic the effect of spin and orbital currents on the electronic structure of bulk CoO in the case of CoO/Pt and CoO/Cu* interfaces. The calculations of the corresponding response tensors in CoO [see figs. S12 and S13 in (*41*)] reveal that the response of dipolar and quadrupolar moments within the gap to the induced orbital exchange fields is up to one order of magnitude larger in absolute value than that of the case of perturbation by spin exchange fields—an effect that originates in the unquenched orbital momentum of Co atoms. Overall, exploiting orbital injection results in more complex, more anisotropic, and more pronounced dynamical response of Co spin and orbital moments when compared with the case of spin injection.

The strong orbital response of CoO to injected OAM can result in a giant OMR amplitude, e.g., through modifications in the anisotropy profile brought by the large nonvanishing current-induced orbital quadrupoles $\langle \{L_i, L_j\} \rangle$. Recently, nonequilibrium orbital quadrupole moments have been shown to mediate an injection of magnetic octupole into altermagnetic materials, driving a novel type of torque on the Néel order parameter $\hat{n}$ (*55*). In CoO, it has been recently shown that the orbital quadrupole moment, arising as a combined result of an externally applied magnetic field and spin-orbit interaction, plays a key role in driving intricate spin-orbital dynamics through the coupling of $\hat{n}$ and $\langle \{L_x, L_y\} \rangle$ (*38*). We show in section S10 of (*41*) that an increased MR signal emerges because the orbital dipole-to-quadrupole conversion does not, in principle, require spin-orbit interaction directly. We thus believe

that the effective orbital quadrupole torques originating from the orbital injection from Cu* can be very efficient and ultimately result in strong absorption of the electrically generated OAM.

One notable feature of CoO, as compared with other materials, is its strong orbital exchange interaction. Our ab initio calculations show that the isotropic antiferromagnetic next-nearest-neighbor spin-spin exchange interaction is by far the largest. However, among the nearest-neighbor exchange interactions, the largest magnitudes are found within the orbital quadrupole-quadrupole subblock [see sections S11 and fig. S14 of (*41*)]. This provides an additional purely orbital channel for energy dissipation by low-energy excitations of orbital degrees of freedom when corresponding dynamics is triggered by the orbital current. We find that below 80 meV, two wide groups of excitation bands are present. Although the exact energetic position of the excitation bands depends sensitively on the structural details of the film and its interfacial properties, the relative difference in the energy of the lower and upper group stems from the qualitatively different nature of the interactions that define them. Indeed, we observe that the lower band is mainly of orbital-quadrupole character, and the upper one is mainly caused by spin excitations. Therefore, the efficient mechanism of orbital excitations by the orbital current, in addition to the coherent torques exerted on the Néel order, can also contribute to a much stronger orbital current absorption by CoO from the Cu* system.

To check the universality of our observation, we have replaced Cu* with Cr as another system that can generate large OAM, and we find that using this metal with weak SOC and a negligible spin Hall effect, a fivefold larger signal is observed in CoO/Cr compared with CoO/Pt [see sections S4 and fig. S5 of (*41*)]. This underscores the applicability of our discovered mechanism and highlights the potential of giant orbital currents to efficiently detect and potentially also manipulate magnetic order through this route. For applications, materials with higher ordering temperature than CoO, and in particular, OAM dominating ferro- and ferrimagnets will be particularly well-suited. Overall, the interaction mechanisms that arise from the combination of the giant orbital current and the large unquenched static OAM in orbital magnets could enable the development of all-orbital devices overcoming the limitations of conventional SOC-mediated processes.

REFERENCES AND NOTES

1. M. N. Baibich *et al.*, *Phys. Rev. Lett.* **61**, 2472–2475 (1988).
2. G. Binasch, P. Grünberg, F. Saurenbach, W. Zinn, *Phys. Rev. B* **39**, 4828–4830 (1989).
3. I. M. Miron *et al.*, *Nature* **476**, 189–193 (2011).
4. S. Bhatti *et al.*, *Mater. Today* **20**, 530–548 (2017).
5. A. Fert, V. Cros, J. Sampaio, *Nat. Nanotechnol.* **8**, 152–156 (2013).
6. K. Everschor-Sitte, J. Masell, R. M. Reeve, M. Kläui, *J. Appl. Phys.* **124**, 240901 (2018).
7. X. Zhang, M. Ezawa, Y. Zhou, *Sci. Rep.* **5**, 9400 (2015).
8. J. Grollier *et al.*, *Nat. Electron.* **3**, 360–370 (2020).
9. T. da Câmara Santa Clara Gomes *et al.*, *Nat. Electron.* **8**, 204–214 (2025).
10. G. Beneke *et al.*, *Nat. Commun.* **15**, 8103 (2024).
11. A. Manchon *et al.*, *Rev. Mod. Phys.* **91**, 035004 (2019).
12. D. Go, D. Jo, H.-W. Lee, M. Kläui, Y. Mokrousov, *Europhys. Lett.* **135**, 37001 (2021).
13. D. Go, D. Jo, C. Kim, H.-W. Lee, *Phys. Rev. Lett.* **121**, 086602 (2018).
14. S. Ding *et al.*, *Phys. Rev. Lett.* **125**, 177201 (2020).
15. K.-J. Lee, V. Cros, H.-W. Lee, *Nat. Mater.* **23**, 1302–1304 (2024).
16. S. Fukami, K.-J. Lee, M. Kläui, *Nat. Phys.* (2025).
17. T. Tanaka *et al.*, *Phys. Rev. B* **77**, 165117 (2008).
18. H. Kontani, T. Tanaka, D. S. Hirashima, K. Yamada, J. Inoue, *Phys. Rev. Lett.* **102**, 016601 (2009).
19. A. Johansson, B. Göbel, J. Henk, M. Bibes, I. Mertig, *Phys. Rev. Res.* **3**, 013275 (2021).
20. S. A. Nikolaev *et al.*, *Nano Lett.* **24**, 13465–13472 (2024).
21. A. Fert, R. Ramesh, V. Garcia, F. Casanova, M. Bibes, *Rev. Mod. Phys.* **96**, 015005 (2024).
22. L. Salemi, P. M. Oppeneer, *Phys. Rev. Mater.* **6**, 095001 (2022).
23. S. Krishnia *et al.*, *Nano Lett.* **23**, 6785–6791 (2023).
24. Y.-G. Choi *et al.*, *Nature* **619**, 52–56 (2023).
25. I. Lyalin, S. Alikhah, M. Berritta, P. M. Oppeneer, R. K. Kawakami, *Phys. Rev. Lett.* **131**, 156702 (2023).
26. A. Bose *et al.*, *Phys. Rev. B* **107**, 134423 (2023).
27. S. Krishnia *et al.*, *APL Mater.* **12**, 051105 (2024).
28. G. Sala, P. Gambardella, *Phys. Rev. Res.* **4**, 033037 (2022).
29. R. Gupta *et al.*, *Nat. Commun.* **16**, 130 (2025).
30. M. I. Katsnelson, Y. O. Kvashnin, V. V. Mazurenko, A. I. Lichtenstein, *Phys. Rev. B* **82**, 100403 (2010).
31. E. Rongione *et al.*, *Nat. Commun.* **14**, 1818 (2023).
32. T. Kampfrath *et al.*, *Nat. Photonics* **5**, 31–34 (2011).
33. R. Lebrun *et al.*, *Nature* **561**, 222–225 (2018).
34. S. Das *et al.*, *Nat. Commun.* **13**, 6140 (2022).
35. M. R. Norman, *Phys. Rev. Lett.* **64**, 1162–1165 (1990).
36. C. T. Chen *et al.*, *Phys. Rev. Lett.* **75**, 152–155 (1995).
37. S. Krishnia *et al.*, *Phys. Rev. Appl.* **24**, 024055 (2025).
38. M. Grzybowski *et al.*, *Phys. Rev. B* **107**, L060403 (2023).
39. W. Wang *et al.*, *Nat. Nanotechnol.* **14**, 819–824 (2019).
40. S. Krishnia *et al.*, *Phys. Rev. Appl.* **16**, 024040 (2021).
41. Materials and methods are available in the supplementary materials.
42. L. Baldrati *et al.*, *Phys. Rev. Lett.* **125**, 077201 (2020).
43. C. Schmitt *et al.*, *Nano Lett.* **24**, 1471–1476 (2024).
44. W. Roth, *Phys. Rev.* **110**, 1333–1341 (1958).
45. S. Saito, K. Nakahigashi, Y. Shimomura, *J. Phys. Soc. Jpn.* **21**, 850–860 (1966).
46. H. Nakayama *et al.*, *Phys. Rev. Lett.* **110**, 206601 (2013).
47. J. Kim, P. Sheng, S. Takahashi, S. Mitani, M. Hayashi, *Phys. Rev. Lett.* **116**, 097201 (2016).
48. S. Ding *et al.*, *Phys. Rev. Lett.* **128**, 067201 (2022).
49. S. Vélez *et al.*, *Phys. Rev. Lett.* **116**, 016603 (2016).
50. G. R. Hoogeboom, A. Aqeel, T. Kuschel, T. Palstra, B. J. van Wees, *Appl. Phys. Lett.* **111**, 052409 (2017).
51. S. R. Marmion, M. Ali, M. McLaren, D. A. Williams, B. J. Hickey, *Phys. Rev. B* **89**, 220404 (2014).
52. J.-Y. Yoon *et al.*, *Nat. Mater.* **22**, 1106–1113 (2023).
53. I. V. Solovyev, A. I. Liechtenstein, K. Terakura, *Phys. Rev. Lett.* **80**, 5758–5761 (1998).
54. A. Boussendel, N. Baadji, A. Haroun, H. Dreyssé, M. Alouani, *Phys. Rev. B* **81**, 184432 (2010).
55. S. Han *et al.*, *Phys. Rev. Lett.* **135**, 076705 (2025).
56. C. Schmitt *et al.*, Data for: Orbital magnetoresistance in the antiferromagnet CoO driven by dynamic orbital angular momentum, Version 1 (Zenodo, 2026); https://doi.org/10.5281/zenodo.18860804.

ACKNOWLEDGMENTS

We acknowledge fruitful discussions with D. Jo and K.-J. Lee. We thank P. Oppeneer for discussions on XAS. We thank D.A. Grave, A. Kay, and A. Rothschild for providing us with the α-Fe_2O_3 thin film. **Funding:** We thank Helmholtz-Zentrum Berlin für Materialien und Energie (HZB) for the allocation of synchrotron radiation beam time, and we acknowledge the financial support by HZB. The authors thank the DFG [Spin+X (A01, A11, B02) TRR 173-268565370 and project 358671374], the Horizon 2020 Framework Programme of the European Commission under FETOpen grant agreement 863155 (s-Nebula); the European Research Council grant agreement 856538 (3D MAGiC); and the Research Council of Norway through its Centers of Excellence funding scheme, project 262633 "QuSpin." This project has received funding from the EU Research and Innovation Programme Horizon Europe under grant agreement 101070290 (NIMFEIA). We also acknowledge the Jülich Supercomputing Centre for providing computational resources under projects jiff40, jiff38, and REPSMANOM. This work was also supported by the EIC Pathfinder OPEN grant 101129641 "OBELIX". This research is a part of the TOPOCOM project, grant agreement 101119608, and ORBIS project, grant agreement 101226840, which are funded by the European Union's Horizon Europe Programme under the Marie Skłodowska -Curie Actions (MSCA). The work at the University of Tokyo was supported by CREST (JPMJCR20C1 and JPMJCR20T2) from JST, Japan, Grant-in-Aid for Scientific Research (S) (JP19H05600), Grant-in-Aid for Transformative Research Areas (JP22H05114) from JSPS KAKENHI, Japan, Grant-in-Aid for Scientific Research (B) (JP24K01326), Grant-in-Aid for Research Activity Start-up (23K19024) from JSPS KAKENHI, Japan, Institute for AI and Beyond of the University of Tokyo, and Sumitomo Chemical. M.K., Y.M., O.G., and J.S. acknowledge support from DFG (Elasto-Q-Mat, TRR 288 – 422213477 projects A12 and A09). **Author contributions:** C.S., S.K., Y.M., and M.K. conceived the project details. The CoO samples were grown by C.S. and L.M. with the assistance of T.Ki. and H.A. and supervised by E.S. C.S. fabricated the devices and performed the electrical measurements with S.K. and E.G. C.S. and S.K. analyzed the data with inputs from T.Ku, Y.M., G.J. and M.K. T.D. and A.K. acquired and analyzed the TEM data supervised by R.D. C.S., E.G., M.Lo, and J.K. performed the XAS measurements, supported by F.K. M.Z., M.Le, D.G., L.V.P., J.S., O.G., and Y.M. provided the theoretical support. R.X. performed supporting electrical measurements. D.T. helped in the sputtering of metal layers. C.S., S.K., L.V.P., Y.M. and M.K. wrote the manuscript. M.K. proposed and supervised the whole project. All authors commented on the manuscript. **Competing interests:** The authors declare no competing interests. **Data, code, and materials availability:** Details for the synthesis and characterization of all materials are in the methods section of (*41*). Data presented in this paper are open access and can be found on an open science framework server (*56*).

SUPPLEMENTARY MATERIALS

science.org/doi/10.1126/science.adw1808
Materials and Methods; Supplementary Text; Figs. S1 to S14; References (*57*–*93*)

Submitted 22 January 2025; resubmitted 23 October 2025; accepted 16 May 2026
10.1126/science.adw1808

Orbital magnetoresistance in the antiferromagnet CoO driven by dynamic orbital angular momentum

Christin Schmitt, Sachin Krishnia, Mahmoud Zeer, Edgar Galíndez-Ruales, Mehak Loyal, Jonas Köhler, Luca Micus, Takashi Kikkawa, Hiroki Arisawa, Thibaud Denneulin, András Kovács, Renyou Xu, Duc Tran, Florian Kronast, Dongwook Go, Leonid V. Pourovskii, Rafal E. Dunin-Borkowski, Timo Kuschel, Marjana Ležai#, Jairo Sinova, Eiji Saitoh, Gerhard Jakob, Olena Gomonay, Yuriy Mokrousov, and Mathias Kläui

Science **393** (6806), . DOI: 10.1126/science.adw1808

Editor's summary

Spin currents can be used to control the magnetic state of ferromagnets, enabling applications such as spin-orbit torque magnetic random-access memory. However, the choice of materials for such applications is restricted by the requirement for strong spin-orbiting coupling, which is necessary to generate the spin currents. Instead of spin, Schmitt *et al*. coupled orbital currents directly to orbital magnetization in CoO/Cu* heterostructures. This approach proved effective in boosting the magnetoresistance signal measured by the researchers. —Jelena Stajic

Science (ISSN 1095-9203) is published by the American Association for the Advancement of Science. 1200 New York Avenue NW, Washington, DC 20005. The title *Science* is a registered trademark of AAAS.